Molecular Crystals and Liquid Crystals
Publication details, including instructions for authors and subscription information:
http://www.tandfonline.com/loi/gmcl20

Nonlinear Optics of Liquid Crystal Light-Valves and Applications

S. Residori [a] , U. Bortolozzo [a] & J. P. Huignard [b]
[a] INLN, Université de Nice-Sophia Antipolis, CNRS, 1361 route des Lucioles, 06560, Valbonne, France
[b] Jphopto, 20 Rue Campo Formio, 75013, Paris, France
Version of record first published: 13 Jun 2012.

To cite this article: S. Residori , U. Bortolozzo & J. P. Huignard (2012): Nonlinear Optics of Liquid Crystal Light-Valves and Applications, Molecular Crystals and Liquid Crystals, 561:1, 225-242

To link to this article: http://dx.doi.org/10.1080/15421406.2012.687516

Mol. Cryst. Liq. Cryst., Vol. 561: pp. 225–242, 2012

ISSN: 1542-1406 print/1563-5287 online
DOI: 10.1080/15421406.2012.687516

Taylor & Francis
Taylor & Francis Group

Nonlinear Optics of Liquid Crystal Light-Valves and Applications

S. RESIDORI,[1,*] U. BORTOLOZZO,[1] AND J. P. HUIGNARD[2]

[1]INLN, Université de Nice-Sophia Antipolis, CNRS, 1361 route des Lucioles, 06560 Valbonne, France
[2]Jphopto, 20 Rue Campo Formio, 75013 Paris, France

We present a review of nonlinear optical properties of liquid crystal light-valves, in particular describing how wave-mixing experiments are implemented in these systems. We show several different applications based on optical wave-mixing occurring in the liquid crystal layer. Slow-light effects are obtained by performing two-wave mixing with a continuous reference beam and a pulse signal, providing group velocities as low as fractions of mm/s. Correspondingly, the group index becomes very large, a property that can be exploited to realize interferometric systems with enhanced sensitivity. Based on the same effect, nonlinear detection of the Sagnac effect and accelerometer systems are realized. Finally, adaptive holography in the liquid crystal light-valve is presented, together with the detection of acoustic waves.

Keywords Adaptive holography; liquid crystals; nonlinear optics; slow-light

1 Introduction

In the last years, spatial light modulators based on liquid crystal technology have emerged as essential components in optical processing systems [1], since they are able to affect the phase or intensity, or both, of an incoming beam, thus permitting the manipulation of information in the optical domain. In an optically addressed spatial light modulator, SLM, the control signal is provided by an optical beam, so that optical parallelism in both the input and the output planes can be exploited [2]. The general structure of an optically addressed SLM comprises two components: the photoreceptor and the electro-optic material, often separated by a dielectric mirror [3]. The input beam activates the photoreceptor which produces a corresponding charge field on the electro-optic material. The read light is modulated in its double pass through the electro-optic element in a retroreflective scheme. Since the readout can provide optical gain, the SLM has also been called a light-valve. Historically, the photoreceptor has been a photoconductor, such as selenium or cadmium sulfide [4], amorphous silicon [5] or GaAs [6], and the electro-optic material has been a nematic liquid crystal layer, either in the parallel or twisted configuration [7].

On the other hand, a lot of research has been devoted to photorefractive materials and their applications, with a large wealth of nonlinear effects discovered and studied [8]. By combining photorefractive materials and nematic liquid crystals, in particular, by using as a photosensitive substrate a monocrystalline $Bi_{12}SiO_{20}$, BSO, cut in the form of a cell

*Address correspondence to S. Residori, INLN, Université de Nice-Sophia Antipolis, CNRS, 1361 route des Lucioles, 06560 Valbonne, France. E-mail: Stefania.Residori@inln.cnrs.fr

wall, transmissive liquid crystal light-valve have been realized, where the input and readout beams may in general coincide [9]. The BSO, well known for its photorefractive properties, is here chosen for its large photoconductivity and transparency in the visible range, together with the possibility of having large monocrystalline samples, with good optical quality and uniform dark resistance.

BSO-made LCLVs have been demonstrated as optical elements with attractive capabilities for laser beam manipulation [10] or coherent image amplification through dynamic holography [11]. The photoconductive and electro- optic properties of the device are separately optimized, so that the excellent photosensitivity comes from the large photoconductivity of the BSO and the large nonlinear response comes from the high birefringence of the nematic liquid crystal layer. The high degree of spatial homogeneity, together with the large optical response, makes these light-valves attractive for operating over a large area and at low light power, with the refractive index controlled in a local and dynamical way, either optically or electrically [12].

We will present in this review the nonlinear optical properties of liquid crystal light-valves and several different applications based on wave-mixing occurring in the liquid crystal layer [13,14]. Slow-light effects are obtained thanks to the resonant character of the two-wave mixing process in the liquid crystal light-valve, LCLV, [15] and are exploited to realize interferometric systems with enhanced sensitivity. Based on the same effect, nonlinear detection of the Sagnac effect and accelerometer systems are realized [16]. Finally, adaptive holography in the LCLV will be presented [17], together with the detection of acoustic waves.

2 The Liquid Crystal Light-Valve: Optical Response

As schematically depicted in Fig. 1, the liquid crystal light-valve, LCLV, is composed of a nematic liquid crystal, LC, in between a glass plate and a photoconductive substrate. The photoconductor is made of a thin slice of the photorefractive crystal $Bi_{12}SiO_{20}$, BSO, here used for its large photoconductivity and transparency in the visible range (maximum sensitivity in the blue-green region of the spectrum). The liquid crystals are planar aligned (nematic director $\vec{n}$ parallel to the cell walls) and the thickness of the LC layer is 15 μm. Transparent electrodes covering the inside surface of the glass plate and the outside surface of the photoconductive plate permit the application of an external voltage V_0 across the

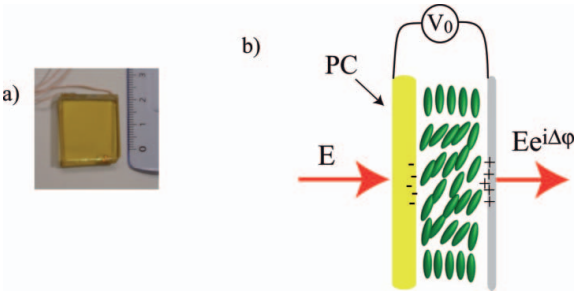

Figure 1. (a) Liquid crystal light-valve, LCLV and (b) its schematic representation: PC is the photoconductive layer, V_0 the applied voltage; when a laser beam of amplitude E pass through the LCLV, at the output it acquires a phase retardation $\Delta\varphi$ that is a function of both V_0 and $|E|^2$.

liquid crystal layer. The photoconductor behaves like a variable impedance, its resistance decreasing when increasing the intensity I of the light impinging on the LCLV. Therefore, the voltage V_{LC} that effectively drops across the LC layer can be expressed ad $V_{LC} = \Gamma V_0 + \alpha I_w$, where V_0 is the a.c. voltage externally applied to the LCLV and Γ, α are phenomenological parameters summarizing, in the linear approximation, the response of the photoconductor (Γ is the dark transfer factor that depends on the impedances of the LCLV dielectric layers) [9].

Under application of the voltage, liquid crystal molecules reorient towards the direction of the electric field [18,19] and, because of liquid crystal birefringence, the molecular reorientation induces a refractive index change for the incoming light. As a result, the beam, when traversing the LC layer, undergoes a phase shift φ, which depends both on the total intensity I of the incident beam and on the applied voltage V_0. The liquid crystal birefringence $\Delta n = n_e - n_0$, n_e and n_o being, respectively, the extraordinary (parallel to $\vec{n}$) and ordinary (perpendicular to $\vec{n}$) refractive index, provides a large refractive index change, $\Delta n = 0.2$, with $n_e = 1.7$ and $n_0 = 1.5$, whereas the large transverse size of the LCLV allows operating over spatially extended wavefronts or whole images.

A typical response of the LCLV showing the measured phase retardation $\Delta\varphi$ as a function of the input intensity I is shown in Fig. 2. The maximum phase shift obtained is as large as 11 π. Saturation is attained when all the molecules are aligned with the direction of the applied field. In the linear part of the response, that is for $I < 10\, mW/cm^2$, the LCLV behaves as a Kerr-like nonlinear medium, providing a refractive index change proportional to the input intensity. The nonlinear coefficient can be calculated as the slope of the characteristic curve in the linear region. This estimation gives $n_2 \simeq -6\ cm^2/W$, the minus sign coming from the defocusing character of the LCLV nonlinearity (the refractive index going from the extraordinary to the ordinary value when molecules orientate from 0 to $\pi/2$).

The response time of the LCLV is given by the collective time needed for the LC layer to reorient, hence, $\tau = (\gamma/K)d^2$, where K is the elastic constant and d the cell thickness, and is of the order of 100 ms. The spatial resolution is determined by the electrical coherence length of the LC, $l_D = \sqrt{K/\Delta\varepsilon}(d/V_0)$, and is of the order of 10 μm.

3 Two-Wave Mixing: Gain and Dispersion Properties

As shown in Fig. 3 two-wave mixing experiment are performed by sending on the LCLV a high intensity pump beam E_p together with a lower intensity signal beam E_s. The two

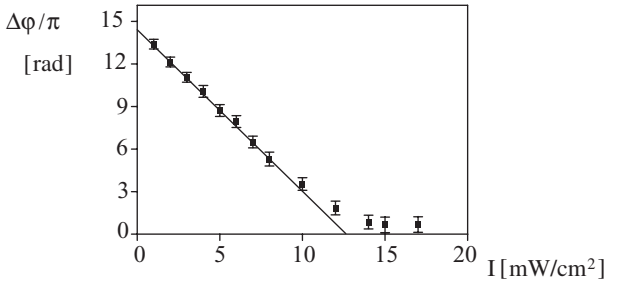

Figure 2. (a) Typical response of the LCLV: the measured phase retardation $\Delta\varphi$ is plotted as a function of the incident light intensity I.

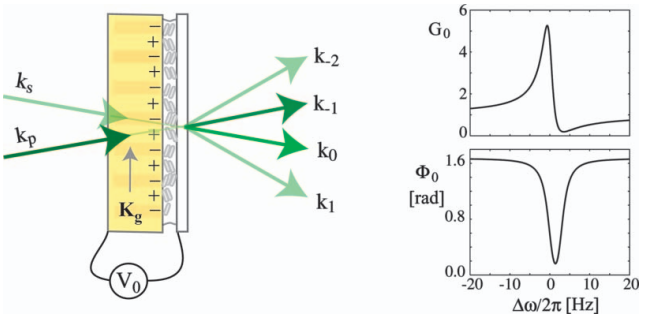

Figure 3. (a) Experimental setup for two-wave mixing experiments in the LCLV; (b) analytically calculated gain G_0 and nonlinear phase shift Φ_0 for the zero order beam as a function of the frequency detuning $\Delta\omega$.

beams interfere in the plane of the photoconductor, thus, give rise to an intensity fringe pattern with a wavevector $\vec{K}_g = \vec{k}_p - k_s$, where $\vec{k}_p$, $\vec{k}_s$ are, respectively, the wavevectors of the pump and signal beam. Correspondingly, a spatially periodic orientation of the LC molecules create a refractive index grating whose amplitude is proportional to the input intensity through the nonlinear coefficient n_2. The two beams may, in general, have slightly different frequencies, hence, a frequency detuning $\Delta\omega = \omega_p - \omega_s$, where ω_p and ω_s are the frequencies of the pump and signal beam, respectively. The beam intensity ratio $\beta = I_p/I_c$ is usually of the order 30, and the fringe spacing $\Lambda = 2\pi/K_g$ is typically 100 μm.

The two beams are scattered by the same grating they are writing in the LC layer, and, thanks to this process, part of the pump photons are transferred in the direction of the signal, which, thus, results amplified. By measuring the signal at the output of the LCLV we have a gain G, to which it is associated a nonlinear phase shift Φ. More precisely, since the LC layer is thin, diffraction occurs in the Raman-Nath regime with several output orders at the exit of the LCLV. The full model consists of a relaxation equation for the refractive index, which corresponds to the relaxation of the LC molecules, which has to be coupled with the Maxwell equation describing the beam propagation inside the LC layer.

The relaxation equation for the molecular orientation dynamics of the LC reads as

$$\tau \frac{\partial n}{\partial t} = -\left(1 - l_D^2 \nabla^2\right) n + n_0 + n_2 |E_{in}|^2, \tag{1}$$

where $l_D = 10\ \mu m$ is the transverse diffusion length, $n_0 = 1.6$ is the constant value of the refractive index given by the average LC orientation under the application of the voltage V_0, and $n_2 \simeq -6\ cm^2/W$ is the equivalent Kerr-like coefficient of the LCLV.

The total electric field at the input of the LCLV can be written as

$$E_{in}(\vec{r}, t) = E_s e^{i[\vec{k}_s \cdot \vec{r} - \omega_s t]} + E_p e^{i[\vec{k}_p \cdot \vec{r} - \omega_p t]} + c.c. \tag{2}$$

The two beams produce an intensity fringe pattern

$$|E_{in}(\vec{r}, t)|^2 = I\left[1 + 2\frac{E_p E_s}{I_T} \cos(\vec{K}_g \cdot \vec{r} - \Delta\omega \cdot t)\right], \tag{3}$$

where $I \equiv |E_s|^2 + |E_p|^2 = I_s + I_p$ is the total input intensity, $\vec{K}_g = \vec{k}_p - \vec{k}_s$ is the grating wave vector and $\Delta\omega = \omega_p - \omega_s$ the frequency detuning between the pump and signal. The fringe pattern induces, on its turn, a photo-induced space charge distribution, hence a molecular reorientation pattern in the LC layer, which creates a refractive index grating with the same wave vector $\vec{K}_g$. Due to self-diffraction, photons from the pump are transferred into the different output orders.

By coupling the above Eq. (1) with the wave propagation equation for the input field, an analytical solution for the m output order field can be found, which reads as [?]

$$\tilde{E}_m = E_m e^{i(\vec{k}_m \cdot \vec{r} - \omega_m t)} + c.c., \tag{4}$$

with $\omega_m = \omega_s - m\,\Delta\omega$ the frequency, $\vec{k}_m = \vec{k}_s - m\,\vec{K}_g$ the wave vector and the amplitude given by

$$E_m = \left[E_s J_m(\rho) + i\,E_p J_{m+1}(\rho) e^{-i\Psi}\right] \cdot e^{i\left[k(n_0 + kn_2 I_T)z + m\left(\frac{\pi}{2} - \Psi\right)\right]}, \tag{5}$$

where J_m is the Bessel function of the first kind and of order m,

$$\rho = \frac{2kn_2 E_p E_s}{\sqrt{\left(1 + l_{LC}^2 K_g^2\right)^2 + (\Delta\omega \cdot \tau_{LC})^2}} d, \tag{6}$$

and

$$\tan\Psi = \frac{\Delta\omega \cdot \tau_{LC}}{1 + l_{LC}^2 K_g^2}. \tag{7}$$

From the above expression Eq. (5), we see that each order m receive two contributions, one is the scattering of the signal and the other is the scattering of the pump onto the refractive index grating. A convenient way of writing the output field is given

$$\tilde{E}_m = \sqrt{G_m} E_s e^{i\Phi_m} e^{i(\vec{k}_m \cdot \vec{r} - \omega_m t)} + c.c., \tag{8}$$

where we define $G_m = |E_m|^2/|E_s|^2$ as the gain amplification factor and Φ_m is the associated nonlinear phase shift. Both G_m and Φ_m can be calculated from Eq. (5).

In Fig. 3b are plotted the gain G_0 and phase Φ_0 calculated for the zero order beam as a function of $\Delta\omega$. We see that the gain is strongly selective in frequency and, corresponding to its narrow bandwidth, there is a strong dispersion, hence, a large phase shift. The gain features permit to obtain optical amplification, while the phase feature permit to obtain slow and fast light phenomena.

3.1 Slow-Light Through Nonlinear Wave-Mixing

To understand the basic mechanism for slow and fast-light, let us first consider only the $m = 0$ order, which coincides with the original propagation direction of the signal,

$$\tilde{E}_0 = \sqrt{G_0} E_s e^{i\Phi_0} e^{i(\vec{k}_s \cdot \vec{r} - \omega_s t)} + c.c. \tag{9}$$

As seen in the previous section, Eq. (5), the envelope amplitude can also be written as

$$E_0 = \left[E_s J_0(\rho) + i E_p J_1(\rho) e^{-i\Psi}\right] e^{i[k(n_0+kn_2 I)z]}, \tag{10}$$

from which we see that two contributions, the scattering of the signal and the scattering of the pump over the index grating, sum up with their relative phases. The final effect is to produce a gain with a narrow frequency bandwidth, to which it is associated a strong dispersion. The maximum gain and phase shift are obtained for $\Delta\omega \sim 0$. In correspondence, a temporally modulated signal will experience a large dispersion, as given by the large slope of the Φ_0 curve on both sides around $\Delta\omega = 0$. By changing the frequency detuning, and thus exploiting either the positive or negative slope of the dispersion curve, both slow and fast-light effects can be achieved.

Indeed, the main idea at the basis of slow-light effects is that of controlling the group velocity of optical pulses, or wave packets [20]. A wave packet is composed by many optical frequencies, each corresponding to a distinct Fourier components propagating with its own phase velocity. For the pulse to propagate without distortion, these components must add in phase for all values of the propagation distance. This implies that the pulse as a whole has to propagate with a group velocity, which is given by

$$v_g = \frac{c}{\left(n + \omega \frac{dn}{d\omega}\right)} \equiv \frac{c}{n_g}, \tag{11}$$

where n_g is the group index characterizing the propagation in the dispersive medium. The group velocity can also be expressed as $c/n_g = d/\tau_g$, with

$$\tau_g = \frac{d\varphi}{d\omega} \tag{12}$$

the group delay provided by the slow-light medium. For large dispersion the group velocity may become very small, giving large slow-light effect, or it may even become negative, producing fast-light effects, that is, the output pulse is anticipated with respect to the input pulse [20]. Therefore, slow and fast-light effects usually make use of the rapid variation of the refractive index close to a material resonance.

Slow-light in the LCLV is obtained by exploiting the resonant character of the two-wave mixing process. Experiments are performed by sending on the LCLV a continuos pump and a time modulated, pulse, signal. The two beams originate from a cw solid state laser, $\lambda = 532\ nm$. They are enlarged and collimated, the beam diameter on the LCLV is 18 mm. The light polarization is linear and parallel to the LC nematic director $\hat{n}_{LC}$. The intensity of the pump beam is fixed to $I_p = 1.8\ mW/cm^2$ whereas the signal beam is time-modulated, by using a spatial-light modulator, to obtain a Gaussian wave packet with a width in between 100 and 200 ms, larger than the LC response time. The center frequency of the signal pulse can be changed by a few Hz with a piezoelectrically driven mirror and its peak intensity is kept much less than the pump intensity, β being usually fixed to 30. The voltage applied to the LCLV is 20 $V\ r.m.s.$ at a frequency of 1 kHz. On each diffracted order, a photodiode records the temporal evolution of the output beam, which is compared to the temporal evolution of the input signal.

Different group delays can be obtained depending on the output order considered and on the frequency detuning $\Delta\omega$ between the pump and signal. Two representative data taken, respectively, on the $m = -2$ and $m = 0$ order are shown in Fig. 4, showing an anticipated, fast-light, and a delayed, slow-light, pulse. Fast-light occurs for $\Delta\omega/2\pi = 3\ Hz$, which

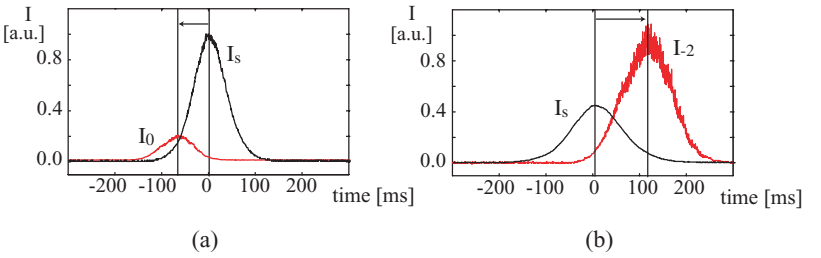

Figure 4. Experimental time dependency of the output pulse (red lines) taken on the (a) $m = 0$ and (b) $m = -2$ diffraction order of the input pulse (black line) showing, respectively, an anticipated (fast-light) and a delayed (slow-light) pulse.

is close to the minimum of the gain, therefore the pulse is attenuated, whereas slow-light is obtained for $\Delta\omega = 0$, which is close to the maximum of the gain. Therefore, the slow-light pulse is not only delayed but also amplified. By fitting each pulse with a Gaussian, we have evaluated the time anticipation as $\Delta t_0 = -65\ ms$ for the fast pulse and the time retardation as $\Delta t_{-2} = 110\ ms$ for the slow pulse. The effective group velocity of each pulse can be determined as $v_m = d/\Delta t_m$, where d is the thickness of the traversed LC layer and Δt_m the group delay of the order m. We obtain $v_0 = -0.21\ mm/s$ for the fast pulse and $v_{-2} = 0.13\ mm/s$ for the slow pulse.

4 Enhanced Sensitivity Interferometers

We have seen that two-wave mixing in the LCLV provides large slow-light effects, hence, a large group index can be associated to the small group velocity characterizing the propagation in the medium. Because of the large group index, we can think as if the effective length of the traversed medium becomes, for the slow pulse, very long. A schematic representation of the effect is shown in Fig. 5a, where a total propagation length of $\Delta L = 1\ m$ is taken into account, within which it is inserted the LCLV with a thickness $d = 15\ \mu m$ of the LC

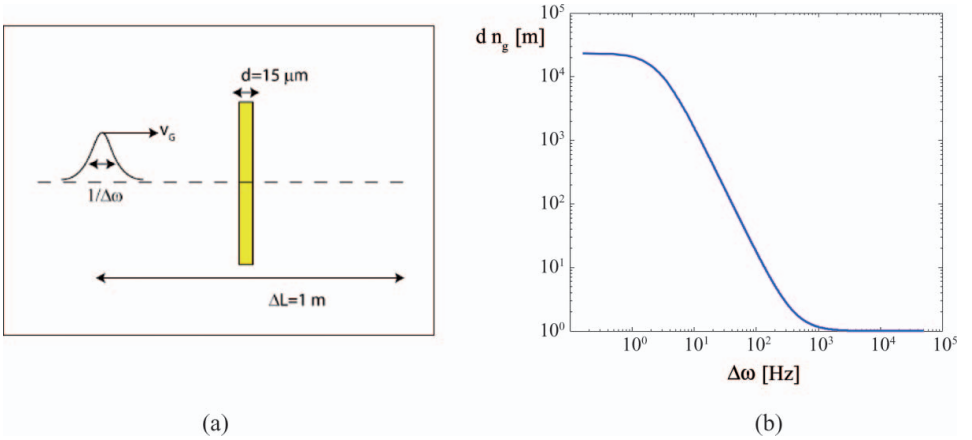

Figure 5. (a) Schematic sketch for the evaluation of the equivalent optical path under the slow-light effect in the LCLV. (b) Equivalent optical path calculated for a propagation distance of $L = 1\ m$ and plotted on log-log scale.

layer. When the LCLV is not operating there is no slow-light effect, hence the total optical path is $\Delta L + dn_0 \simeq \Delta L$, while in the presence of the slow-light effect the effective optical path becomes $\Delta L + dn_g \simeq dn_g \gg \Delta L$.

In Fig. 5b the equivalent optical path, calculated for $\Delta L = 1\ m$, is plotted as a function of the frequency $\Delta\omega$ characterizing the spectral contents of the pulse. We see that equivalent optical paths as large as $10^4\ m$ are obtained as long as the frequency disturbances $\Delta\omega$ are inside the frequency bandwidth of the resonant process inducing slow-light effects in the LCLV. When $\Delta\omega$ increases, this eventually brings the process outside resonance and the optical path goes down to $\Delta L = 1\ m$, corresponding to the physical distance.

4.1 Slow-Light Based Mach-Zehnder Interferometer

Slow-light can be used to enhance the sensitivity of certain types of interferometers [21]. In the LCLV, we can exploit the large group index, hence, the large amplification of the equivalent optical path, to build interferometers with enhanced spectral resolution, the enhancement factor being equivalent to the group index of the slow-light medium. As an example, we have realized a Mach-Zehnder interferometer where, in one arm, we have inserted the LCLV [22]. The setup is schematically represented in Fig. 6a. A pump beam is incident on the LCLV and the interferometer is aligned along the direction of the $m = 0$ output order. If we introduce a small frequency perturbation Ω on the input signal, the transmission of the interferometer is given by

$$T = \frac{1}{2}\left[1 + \cos\Delta\varphi\right] \tag{13}$$

where the total phase difference $\Delta\varphi$ is given by the optical path difference ΔL between the two arms of the interferometer and by the slow-light nonlinear phase retardation Φ_0, which, as we have seen before, is a function of the frequency detuning Ω. If the frequency perturbation is small with respect to the bandwidth of the two-wave-mixing, $\Omega < 1/(2\tau_{LC})$,

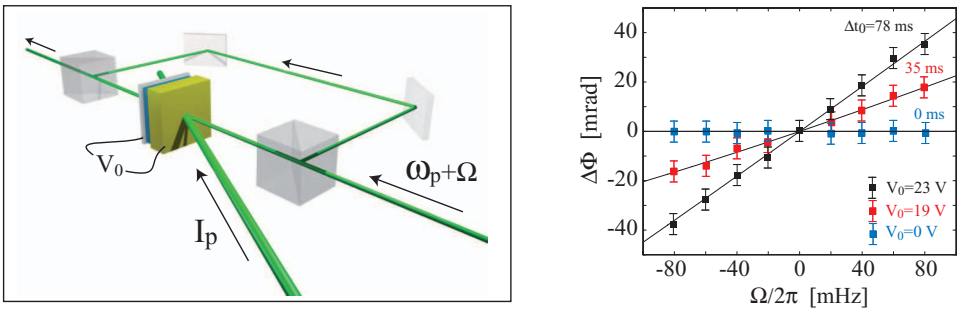

(a) (b)

Figure 6. (a) Schematic diagram of a Mach-Zehnder interferometer with the LCLV operating as a slow-light medium; BS: beam-splitters, M: mirrors. (b) Phase shift detected by the interferometer as a function of the perturbation frequency Ω for different voltages V_0 applied to the LCLV and, correspondingly, increasing group delay Δt_0.

we can write

$$\Phi_0(\Omega) \simeq \Phi_0(0) + \left[\frac{\partial \Phi_0}{\partial \Omega}\right]_0 \Omega = \Phi_0(0) + \Delta t_0\, \Omega. \tag{14}$$

Since the group delay is much larger than $\Delta L/c$ (for example, for $\Delta L = 1\ m$ we have $\Delta L/c \sim 10^{-6}\ s$), we can neglect the linear contribution and the total phase shift can be written as

$$\Delta\varphi \simeq \Phi_0(0) + \Delta t_0 \Omega, \tag{15}$$

therefore, the spectral sensitivity of the interferometer is directly related to the group delay Δt_0 experienced by the zero-th order of diffraction

$$T = \frac{1}{2}\left[1 + \cos(\Delta t_0 \Omega + \Phi_0(0))\right]. \tag{16}$$

Thanks to the tunability of $\Phi_0(0)$ through V_0, in the experiment we can fix $\Phi_0(0) = \pi/2$, so that $T \propto \sin \Delta t_0\, \Omega$ and for small frequency perturbations the detection becomes linear, $T \simeq \Delta t_0\, \Omega$, with Δt_0 typically of the order of $100\ ms$.

In Fig. 6b we report the phase change $\Delta\phi$ measured at the output of the interferometer when a small frequency perturbation Ω, created by a piezoelectrically driven mirror, is added on the signal beam. While the interferometer shows no sensitivity with the LCLV switched off, $V_0 = 0$, we see that the sensitivity largely increases for increasing V_0. The slopes of the detection curves are given by the corresponding group delay provided by the slow-light process in the LCLV.

4.2 Wave-Mixing with Different Polarization States

Due to the intrinsic anisotropic features of the LC, when the wave-mixing is performed with different polarization states the interaction between pump and signal also displays an anisotropic character. Indeed, the beam-coupling occurs only for extraordinary waves, while ordinary waves pass unaltered through the LC layer, except for experiencing a constant refractive index n_o.

By performing two-wave mixing experiments with the polarization of the signal at 45° with respect to the extraordinary axis $\hat{e}$, we have to decompose the input into an ordinary (P) and an extraordinary (S) components, the two behaving quite differently: while the pump and the S-polarized component interact through the wave-mixing process, the P-polarized component do not interact with the medium. As a result, the S component experiences a gain and a nonlinear phase shift, acquiring a group velocity $v_{ge} = d/\tau_g$, where $\tau_g = -d\Phi/d\omega$ is the group delay provided by the slow-light effect, while the P component only sees the ordinary index n_o, and, thus, has a group velocity $v_{go} = c/n_o$. This effect produces a large slow-light birefringence, that is, very different group indices for the ordinary and the extraordinary pulse [23].

The experimental setup, shown in Fig. 7a, is essentially the same as for the two-wave mixing, but with the input signal polarized at 45° with respect to $\hat{e}$. At the output of the LCLV, a polarizing cube splitter, PBS, separates the S and P components of the pulse and two photodiodes record their individual time dependency. Fig. 7b shows two experimental output pulses recorded for the S and P components of the signal and for a spatial period of the grating $\Lambda_g = 250\ \mu m$. We can see that the S pulse is delayed with respect to the P pulse, with a relative retardation as large as $\Delta t = 160\ ms$. The relative delay between the

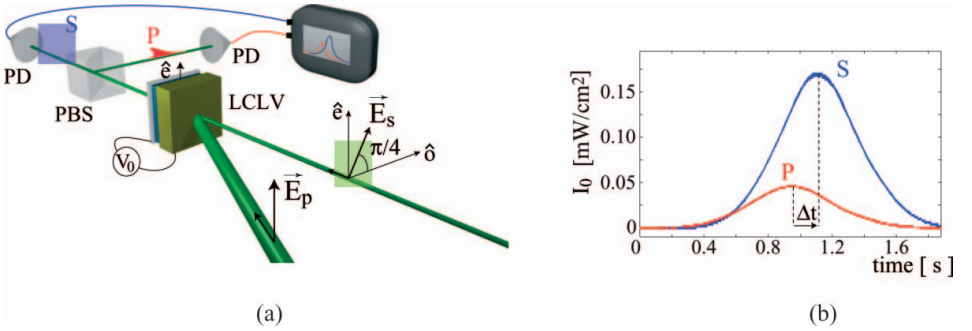

Figure 7. (a) Experimental setup: the pump $\vec{E}_p$, polarized along $\hat{e}$, is sent onto the liquid crystal light-valve (LCLV) together with the input pulse $\vec{E}_s$, polarized at 45° with respect to $\hat{e}$; a polarizing cube (PBS) splits the output signal into its S and P components (parallel, respectively, orthogonal to $\hat{e}$), each detected by a photodiode (PD). (b) Experimentally recorded S and P output pulses; $V_{0peak} = 30$ V frequency 70 Hz.; the time delay between S and P is $\Delta t = 160\ ms$.

S and P output pulses can be controlled by changing the voltage V_0 applied to the LCLV, and goes from 0 to a maximum of 160 ms.

Theoretically, the group index for the ordinary and the extraordinary wave can be calculated calculated by generalizing to a vectorial description the scalar theory of the wave-mixing in the LCLV [23]. In Fig. 8a are plotted n_o and n_e vs the frequency detuning $\Delta\nu = \nu_p - \nu_s$ of the TWM, $\nu_p = \omega_p/2\pi$ and $\nu_s = \omega_s/2\pi$. The two-beam coupling contribution is calculated for $n_c = 1.62, n_2 = -6\,cm^2/W$, $I_p = 3\,mW/cm^2$, $I_s = 0.1\,mW/cm^2$, $\tau_{LC} = 120\ ms$. While n_o always shows the normal LC dispersion, n_e shows a sharp resonance around $\nu = 0$. In Fig. 8b are plotted the corresponding group index. While n_o remains unchanged, and the ordinary group index $n_{go} \simeq n_o$, the rapid variation of n_e close to $\Delta\nu = 0$ produces a large dispersion, so that the extraordinary group index $n_{ge} \simeq n_e + \nu_s(dn_e/d\nu_s)$ becomes very large and a large slow-light effect occurs for the extraordinary wave. Correspondingly, the slow-light birefringence $n_{go} - n_{ge}$ is obtained.

4.3 *Common-Path Interferometer*

The slow-light birefringence, SLB, effect can be exploited to realize a common-path polarization interferometer, where the sensitivity is enhanced by the large difference in the

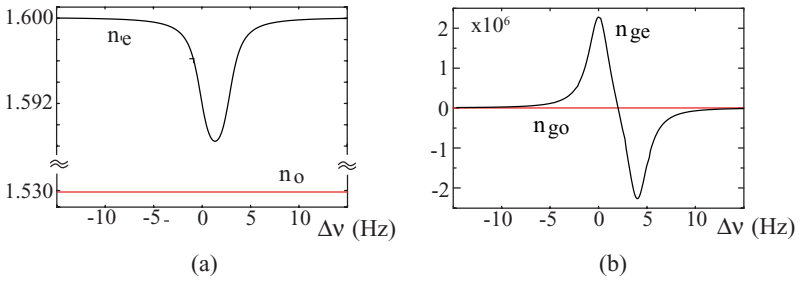

Figure 8. (a) LC refractive indices n_o and n_e vs the frequency detuning $\Delta\nu$ between pump and signal; (b) corresponding group index n_{ge} and n_{go}.

group index for the ordinary and extraordinary waves. The experimental setup is essentially the same as represented in Fig. 7a, but with the PBS replaced by an analyzer, that is, a polarizer with its axis orthogonal to the polarization of the input signal. After the analyzer, the interference pattern made by the S and P components is recorded by a CCD camera, whereas a local intensity signal on the P component, $I_{out\,P}$, is measured by a photodiode.

Before arriving at the LCLV, the input signal is reflected by a piezo-driven mirror, which is made to oscillate at a low frequency $\Omega = 0.16\ Hz$ and with a small amplitude, $\lambda/20$, square wave. The aim is to image the surface of the vibrating mirror and to detect the small displacements accompanying the vibration. In Fig. 9a we show the interference pattern obtained after the analyzer by switching on the pump beam. The diameter of the pump, marked by a dashed line, is made smaller than the signal, at the purpose of highlighting on the same image the effect of the beam-coupling in the LCLV. In Fig. 9b it is shown the temporal evolution of the intensity $I_{out\,P}$ recorded by the photodiode. The lower trace is measured without the pump, the upper trace is recorded in the presence of the pump. We can note the large amplification of the phase change that is induced by the SLB. We see, also, that the interferometer is sensitive to phase variations, that is, I_{out} is proportional to the instantaneous frequency $d\varphi/dt$, hence, providing the derivative of the phase modulation.

Indeed, the sensitivity of the SLB interferometer is determined by the group delay of the the slow-light effect undergone by the extraordinary component. The sensitivity can be analytically calculated by projecting the output field along the analyzer axis, $I_{out\,P} \equiv |\langle \vec{E}_{out}|\vec{P}\rangle|^2$, with $\vec{E}_{out} = E_s/\sqrt{2}e^{ikdn_o}\hat{o} + E_e e^{ikdn_e}\hat{e}$ and the extraordinary component given by [23]

$$E_e = \frac{E_s}{\sqrt{2}} + i\frac{E_p}{2}\frac{kdn_2\sqrt{2I_pI_s}}{\sqrt{1+(2\pi\Delta\nu\cdot\tau_{LC})^2}}e^{-i\psi}. \tag{17}$$

The theoretically calculated $I_{out\,P}$ is plotted in Fig. 10 as a function of $\Delta\nu$ together with the experimental points measured by introducing a frequency detuning between pump and signal. The slope of the curve in the linear slow-light region ($\Delta\nu > 0$) gives the sensitivity of the SLB interferometer.

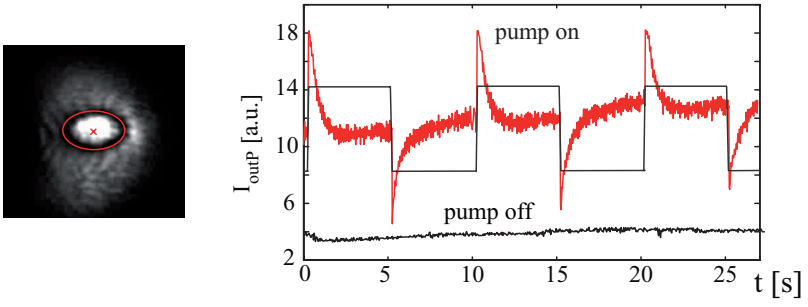

(a) (b)

Figure 9. (a) Polarization interference pattern after the analyzer; the dashed line marks the diameter of the pump beam; the cross indicates the location of the photodiode; (b) temporal evolution of $I_{out\,P}$; lower trace: pump off, upper trace: pump on, dashed line: signal driving the piezo-mirror (phase modulation).

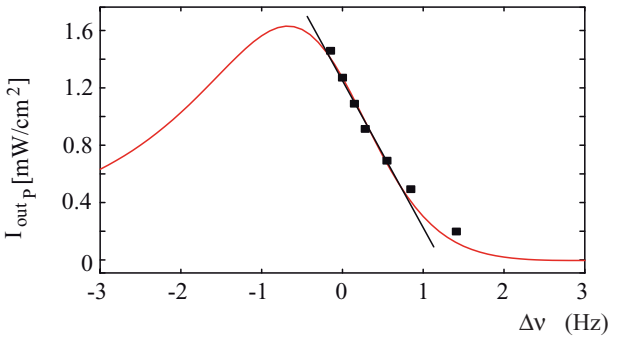

Figure 10. Sensitivity of the slow-light birefringence interferometer: output intensity I_{out_P} vs $\Delta\nu$; solid line: theoretical curve, black squares: experimental points.

4.4 Accelerometer Based on Sagnac Effect

Sagnac effect is due to nonreciprocity, that is, to the different optical path of two counter-propagating waves in a rotating ring interferometer, and has been widely investigated, on one side, for its fundamental interest in theoretical physics and in geophysics and, on the other hand, for its important applications in rotation sensing and inertial guidance [24,25]. Sagnac effect is, indeed, the basis of rotationally sensitive lasers, or optical gyroscopes. The possibility of enhancing Sagnac detection by using slow-light media has been recently considered [26], slow-light usually occurring close to a material resonance where the refractive index varies rapidly with phase changes. Other approaches towards Sagnac detection resort to the possibility of employing nonlinear media [27,28,29].

Based on the nonlinear and adaptive detection in the LCLV, we have realized a Sagnac interferometer where the two-wave mixing is performed between the clockwise and counterclockwise waves traveling along the different paths of interferometer [16]. The setup is shown in Fig. 11a. An input beam, $\lambda = 532\ nm$, intensity $I = 3\ mW/cm^2$, polarized linearly along $\hat{e}$, is divided in two beams of equal intensity, entering the interferometer through the beam-splitter, BS. One beam, A_{CW}, is directed clockwise and the other beam,

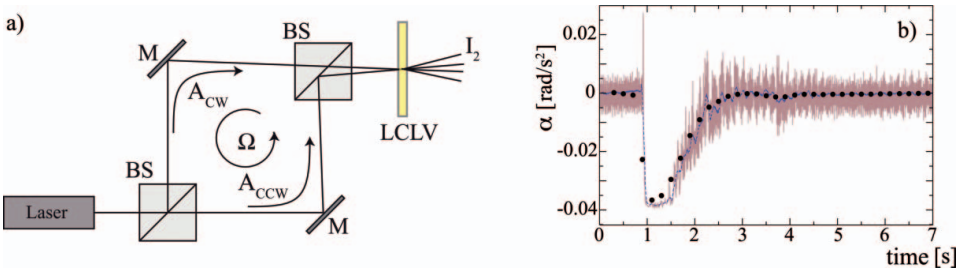

Figure 11. (a) Experimental setup for Sagnac effect detection: the beam-splitter BS directs one beam, A_{CW}, clockwise and the other beam, A_{CCW}, counterclockwise; the second BS sends the two beams to interfere in the LCLV; the intensity I_2 is measured by a photodiode and converted into angular acceleration $\alpha = \dot{\Omega}$. (b) Measured α versus time; continuous line: signal detected by the photodiode; dashed line: same signal filtered with a bandwidth of 25 Hz; dots: measurements in the motionless laboratory frame.

A_{CCW}, counterclockwise. At the second BS the two beams are sent to interfere and perform wave-mixing in the LCLV. The angle between the two interfering beams is 3 *mrad*, corresponding to a fringe spacing of about 100 μm. The whole experiment is mounted on a rotating platform, with $\Omega(t)$ the angular velocity. When the setup rotates, the two beams A_{CW} and A_{CCW}, before interfering in the LCLV, acquire a differential phase shift $\Phi(t)$ due to the Sagnac effect. The intensity I_m of the m output order is measured with the photodiode PD and, in the slow-light regime, is directly converted in angular acceleration $\alpha = \dot{\Omega}$.

The signal is measured with the photodiode on one of the output orders and is compared with the measurements done in the motionless laboratory frame by using a chronometric tagged tape around the turntable and a laser-photodiode detection system [16]. In Fig. 11b an example of the angular acceleration $\alpha(t)$ detected by operating the interferometer at low rotation frequency and by measuring the output intensity I_2 on the $m = 2$ order. α is made to change by impressing a single small impulse to the turntable and then letting it to go to rest. The signal measured with the photodiode (solid line) is compared with the angular acceleration measured in the motionless laboratory frame Sagnac accelerometer. The filtered signal is very well proportional to the acceleration measured in the laboratory frame.

We have performed several measurements by varying the acceleration and for two different areas of the interferometer. The intensity scales very well linearly with the angular acceleration, so that, by calibrating the measurements, we can directly convert I_2 in angular acceleration units. The minimal acceleration that can be detected can be estimated by considering the photon shot noise, and is of the order of 10 $microrad/sec^2$.

The theoretical description accounts for the wave-mixing between the two beams in the interferometer. In the moving frame of reference of the nonlinear medium, the refractive index is described by the relaxation equation, Eq. (1). The total field at the LCLV is the sum of the two counterpropagating beams

$$E_{in}(\mathbf{r}, t) = A_{CW} e^{i(\mathbf{k_1}\cdot\mathbf{r}+\varphi_1-\omega_0 t)} + A_{CCW} e^{i(\mathbf{k_2}\cdot\mathbf{r}+\varphi_2-\omega_0 t)}, \tag{18}$$

where ω_0 is the laser pulsation in the proper moving frame and $\Phi(t) = \varphi_1 - \varphi_2$ is the Sagnac phase shift. In the case of constant rotation velocity the Sagnac phase shift is given by the well-known expression $\Phi_0 = 8\pi\, A\Omega_0/(\lambda_0\, c)$, where A is the area enclosed by the interferometer and Ω_0 is the angular velocity.

The solution for the dynamical equation, Eq. (1), is obtained by considering a sinusoidal index grating with a time dependent amplitude and phase

$$n = n_A + n_B(t)\cos\left[(\mathbf{k_1} - \mathbf{k_2})\cdot\mathbf{r} + \varphi(t)\right] \tag{19}$$

where $n_A = n_0 + n_2(|A_{CW}|^2 + |A_{CCW}|^2)$ is the homogeneous index of refraction renormalized by the total light intensity, $n_B(t)$ and $\varphi(t)$ are the amplitude and, respectively, the phase of the index grating generated by the wave-mixing. In the case of constant angular velocity $\Omega(t) = \Omega_0$ the solution is $n_B = 2\, n_2\, A_{CW}\, A_{CCW}$ and $\varphi(t) = \Phi_0$, which are time independent. In the general case of non constant angular velocity $\Omega(t)$, the intensity for the m output order can be calculated and can be shown to be proportional to [30]

$$I_m \propto J_{m-1}(\rho)\, J_m(\rho)\ \sin\left[\Phi(t) - \varphi(t)\right], \tag{20}$$

where J_m is the Bessel function of the first kind and of order m, $\rho = (\omega_0 n_B d)/c$ is proportional to the grating amplitude. We see from the above equation, Eq. (20), that for constant

angular velocity, $\varphi(t) = \Phi(t) = \Phi_0$, there is no change of the output intensity. In this operating regime the two-wave mixing exactly compensates the relative phase shift between the two counterpropagating beams [17], with the nonlinear medium acting as an hologram that adapts to any external phase change [31,32].

We consider now the case of a small angular acceleration, with the angular velocity expressed as $\Omega(t) = \Omega_0 + \alpha t$. The leading term for the Sagnac phase shift can be calculated and is given by [33]

$$\Phi(t) = \frac{8\pi A}{\lambda_0 c}\left[\Omega_0 + \alpha\left(t - \frac{P}{c}\right)\right], \tag{21}$$

where P is the perimeter of the interferometer. When the interferometer operates in the slow-light regime, that is, the frequency changes are inside the bandwidth of the nonlinearity, the LCLV provides a direct detection of phase variations. Under these conditions, by inserting Eq. (20) in Eq. (1), we can calculate the intensity for the generic output order m and we obtain

$$I_m \propto J_{m-1}(\rho)\, J_m(\rho)\, \frac{8\pi A\tau}{\lambda_0 c}\, \alpha, \tag{22}$$

where τ is the response time of the nonlinear medium. In this regime the output intensity is directly proportional to the angular acceleration α.

5 Adaptive Holography

The main objective of the adaptive interferometry is to detect frequency phase modulations of optical beams with complex wavefronts, such as speckle beams, characterized by low frequency noise fluctuations. This problem is important when phase measurements are to be performed under environmental noisy conditions, as for imaging through the atmosphere, or turbid media or biological tissues. The approach of adaptive holography is that of using a nonlinear process in order to produce a self-adapting hologram, that is, an hologram able to follow the low frequency disturbance and to react in order to maintain the optimum detection condition [31]. An important property of the adaptive hologram is the narrow optical bandwidth, which gives the ability of the system to reject low frequency noise. Because slow-light in the LCLV is related to a narrow frequency bandwidth for the gain, nonlinear wave-mixing processes in the LCLV are naturally good candidates for realizing adaptive holographic systems.

The experimental setup is shown in Fig. 12a. By means of a piezoelectrically driven mirror the signal beam E_s is phase modulated with a sinusoidal oscillation at a frequency $\Omega/2\pi = 1\ kHz$, much greater than the bandwidth of the two-wave-mixing in the LCLV, and with a small amplitude Δ. The signal beam is sent onto the LCLV together with a reference beam E_R. The optical power of the output beams is measured through a photodiode and a lock-in amplifier synchronized to the frequency Ω of the phase modulation. The amplitude of the phase grating that is generated by the two-wave-mixing inside the LC layer is given by

$$\varphi = 2kdn_2 E_R E_s J_0(2k\Delta). \tag{23}$$

Because of the large value of the LCLV nonlinear coefficient n_2, the process is very efficient and the output diffracted beams are easily detected. In particular, the output optical power

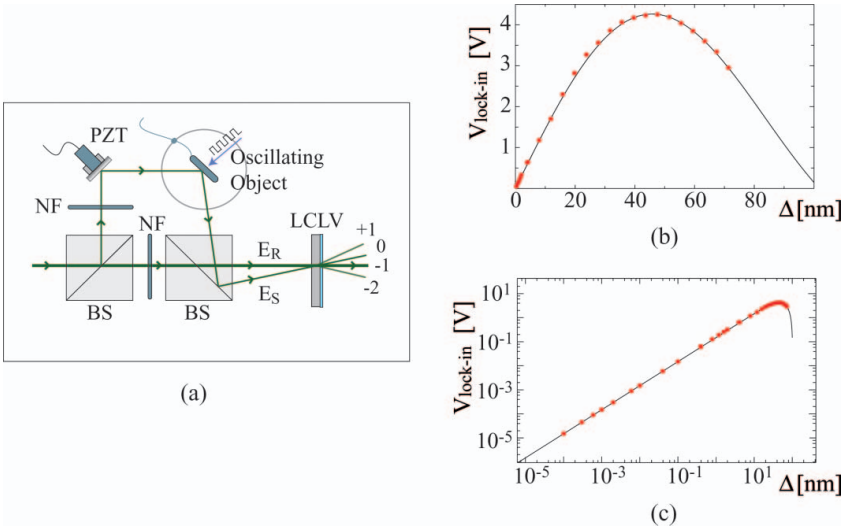

Figure 12. (a) Schematic diagram of the adaptive holographic system using the LCLV as a narrow frequency bandwidth medium; NF: neutral density filters, PZT: piezo-electrically driven mirror. (b) Signal $V_{lock-in}$ detected on the $m = -1$ order as a function of the mirror displacement Δ; c) the same data are plotted in logarithmic scale.

at the frequency Ω can be calculated and it is given by

$$\hat{P}_m(\Omega) = 4P_R e^{-\alpha D} K J_m(\varphi) J_{m+1}(\varphi) J_1(2k\Delta), \tag{24}$$

where m is the order of diffraction, $D = 1\ mm$ the thickness of the photoconductor and $\alpha = 0.3\ cm^{-1}$ its absorption coefficient. The ratio between the intensity of the reference and signal beam is K and J_m is the Bessel function of first kind and order m.

An important characteristic of the adaptive holography is that when the amplitude of the phase modulation is small the detection is always linear in Δ, this at variance with standard interferometers where the detection is linear only for precise values of the optical path difference between the reference and signal beam. The sensitivity of the system is obtained by considering the photon shot-noise. The signal to noise ratio in this case is given by [17]

$$SNR = \sqrt{\frac{2\eta P_R}{\hbar\omega\Delta f}} e^{\frac{-\alpha D}{2}} \frac{K J_m(\varphi) J_{m+1}(\varphi)}{\sqrt{K^2 J_m^2(\varphi) J_{m+1}^2(\varphi)}} 2k\ \Delta, \tag{25}$$

where $\eta = 0.4$ is the quantum efficiency of the photodiode and $\Delta f = 1\ Hz$ is the bandwidth of the electronic detection system. The maximum signal to noise ratio is obtained for $m = -1$ and the minimum detectable phase is of the order of $7\ nrad/Hz^{1/2}$. In Fig. 12b, the detected signal $V_{lock-in}$ is plotted as a function of the mirror displacement Δ, for the $m = -1$ order, for which the theoretical curves predict the maximum sensitivity [17]. The intensity of the optical beam was $3\ mW/cm^2$ and $K = 5$. In Fig. 12c the same data are

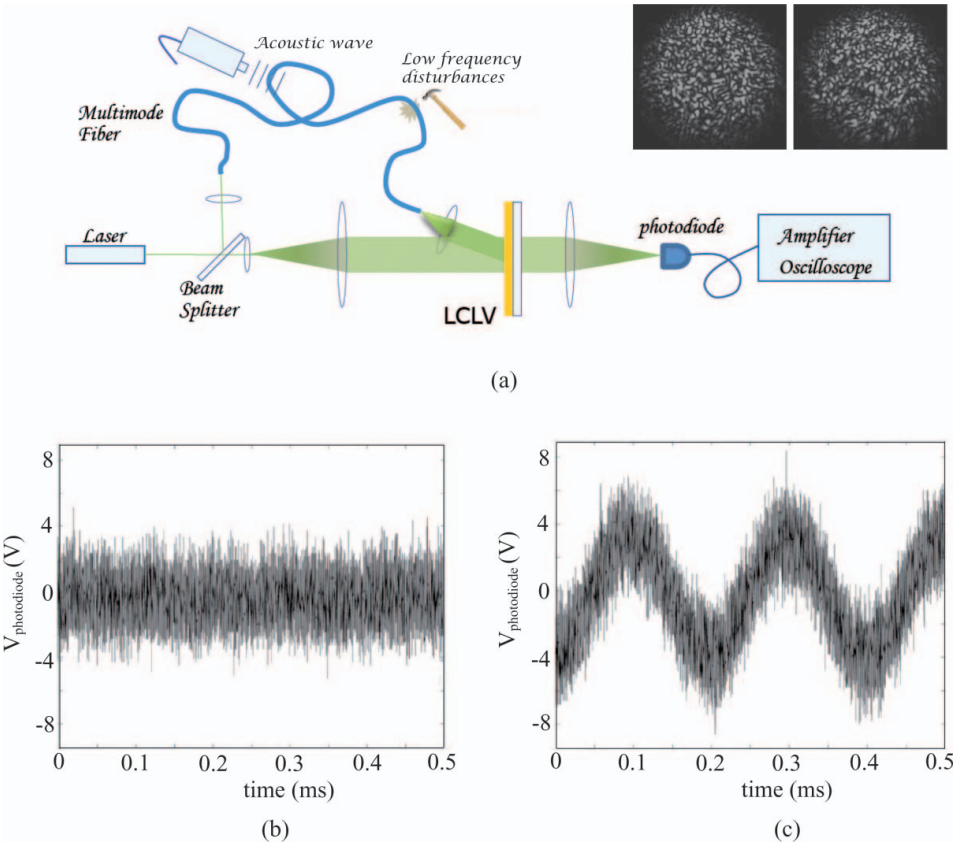

Figure 13. (a) Schematic setup for the detection of phase modulations of a speckles field. In the inset, the speckles field at the output of the multimode fiber is shown at two different instant times; the time separation between the two images is 0.2 *s*. Signal $V_{photodiode}$ detected as a function of time in the case of (b) a standard Michelson interferometer and (c) after the LCLV in the adaptive holographic system.

plotted in logarithmic scale. We see that the detection is linear for small displacements and that mirror displacements as small as 0.1 *pm* are detected.

Finally, in order to test the ability of the system to work with complex wavefronts, we have performed an experiment in which we take as signal the optical field distribution at the exit of a multimode fiber. The setup is sketched in Fig. 13. A high frequency modulation is created by sending on the fiber an acoustic wave at $\Omega/2\pi = 5\ KHz$ and low frequency perturbations are induced by local, and small, disturbances, induced, for example, by touching the fiber. At the exit of the fiber, the optical field distribution is a speckles pattern with a slow dynamics, as shown in the inset of Fig. 13. In the case of a classical interferometer the phase modulations of the signal are completely hidden by the noise, as shown in Fig. 13a. In the case of adaptive holography, the two-wave mixing in the LCLV provides a narrow frequency bandwidth that filters out noise low frequency noise fluctuations, and the acoustic wave modulating the signal can be clearly distinguished, as it appears evident in Fig. 13b.

6 Conclusions

In conclusion, we have seen that nonlinear optical interactions can be efficiently implemented in liquid crystal light-valves by performing wave-mixing experiments. Beam amplification and slow-light effects are obtained, with a group velocity as low as fractions of mm/s. This property can be exploited to enhance the sensitivity of certain types of interferometers. We have shown, as an example, the detection performances of a slow-light based Mach-Zehnder interferometer. Then, a common-path polarization interferometer has been realized based on the slow-light birefringence effect, showing high sensitivity to phase changes. Always based on the slow-light process in the LCLV, nonlinear detection of the Sagnac effect has been achieved, where the optimum detection condition is adaptively maintained. Finally, by using the narrow frequency bandwidth associated with slow-light, self-adaptive interferometric systems have been implemented and tested for the detection of small displacements. The self-adaptive character of the nonlinear process can be exploited to perform phase detection with spatially complex wavefronts, such as speckles or distorted fields, and to detect acoustic waves in noisy environment.

References

[1] Efron U., & Liverscu G. (1995). Spatial Light Modulator Technology: Materials, Devices and Applications, Dekker: New York.
[2] Collings N. (1988). Optical Pattern Recognition Using Holographic Techniques, Addison-Wesley: Reading, MA.
[3] Armitage D., Thackara J. I., & Eades W. D. (1989). *Appl.Opt.*, *28*, 4763.
[4] Grinberg J., Jacobson A., Bleha W. P., & Miller L. (1975). *Opt. Eng.*, *14*, 217.
[5] Ashley P. R., & Davis J. H. (1978). *Appl. Opt.*, *26*, 241.
[6] Akhmanov S. A., Vorontsov M. A., & Ivanov V. Yu (1988). *JETP Lett.*, *47*, 707.
[7] Efron U., Wu S. T., & Bates T. D. (1986). *J. Opt. Soc. Am. B*, *3*, 247.
[8] Gunter P., & Huignard J. P. (2006). Photorefractive Materials and their Applications 1, 2 and 3, Springer: New York.
[9] Aubourg P., Huignard J. P., Hareng M., & Mullen R. A. (1982). *Appl. Opt.*, *21*, 3706.
[10] Sanner N., Huot N., Audouard E., Larat C., Huignard J. P., & Loiseaux B. (2005). *Opt. Lett.*, *30*, 1479.
[11] Brignon A., Bongrand I., Loiseaux B., & Huignard J. P. (1997). *Opt. Lett.*, *22*, 1855.
[12] Bortolozzo U., Residori S., Petrosyan A., & Huignard J.P. (2006). *Opt. Commun.*, *263*, 317.
[13] Bortolozzo U., Residori S., & Huignard J. P. (2006). *Opt. Lett.*, *31*, 2166.
[14] Residori S., Bortolozzo U., & Huignard J. P. (2009). *Appl. Phys. B*, *95*, 551.
[15] Residori S., Bortolozzo U., & Huignard J.P. (2008). *Phys. Rev. Lett.*, *100*, 203603.
[16] Residori S., Bortolozzo U., & Huignard J. P. (2011). *Opt. Lett.*, *36*, 520.
[17] Bortolozzo U., Residori S., Huignard J. P. (2009). *Opt. Lett.*, *34*, 2006.
[18] Khoo, I. C. (2007). Liquid Crystals: Physical Properties and Nonlinear Optical Phenomena (second edition), Wiley Interscience: New York.
[19] De Gennes P. G., & Prost J. (1993). The Physics of Liquid Crystals, Oxford Science Publications: Clarendon Press.
[20] Boyd R. W., & Gauthier D. J. (2002). Progress in Optics, edited by E. Wolf, Vol. 43, Elsevier Science: Amsterdam, 497.
[21] Shi Z., Boyd R. W., Gauthier D.J., & Dudley C. C. (2007). *Opt. Lett.*, *32*, 915.
[22] Bortolozzo U., Residori S., & Huignard J. P. (2010). *Laser Photonics Rev.*, *4*, 483.
[23] Bortolozzo U., Residori S., & Huignard, J. P. (2010). *Opt. Lett.*, *35*, 2076.
[24] Post, E. J. (1967). *Rev. Mod. Phys.*, *39*, 475.
[25] Arditty H. J., & Lefèvre, H. C. (1981). *Opt. Lett.*, *6*, 8.
[26] Salit, M., Pati, G. S., Salit, K., & Shahriar, M. S. (2007). *J. Mod. Opt.*, *54*, 2425.

[27] Kaplan, A. E., & Meystre, P. (1981). *Opt. Lett.*, *6*, 12.
[28] Fischer, B., & Sternklar, S. (1985). *Appl. Phys. Lett.*, *47*, 1.
[29] Yeh, P., McMichael, I., & Khoshnevisan, M., *Appl. Opt.*, *25*, 1029–1030 (1986).
[30] Bortolozzo U., Residori S., & Huignard J. P. (2010). *C. R. Physique*, *10*, 938.
[31] Kamshilin A. A., Romashko R. V., & Kulchin Y. N. (2009). *J. Appl. Phys.*, *105*, 031101.
[32] Stepanov S. I., Sokolov I. A., Vlad V. I., Popa D., & Apostol I. (1990). *Opt. Lett.*, *15*, 1239.
[33] Neutze R. (1995). *Phys. Rev. A*, *51*, 5039.